

Reconstruction of localized force distributions in cells and tissues from substrate displacements using physically-consistent regularization

Joshua C. Chang and Yanli Liu and Tom Chou

Epidemiology and Biostatistics Section, Rehabilitation Medicine,

Clinical Center, The National Institutes of Health, Bethesda MD, 20892 and

Depts. of Biomathematics and Mathematics, UCLA, Los Angeles, CA 90095-1766

We develop a method to reconstruct, from measured displacements of the underlying elastic substrate, the spatially dependent forces that cells or tissues impart on it. Since these sources of force typically arise from focal adhesions, which are localized and can exist only within the footprint of the cell or tissue, they are compactly supported. We solve this inverse problem using methods of L^1 optimization often used in image segmentation. In addition to the standard quadratic data mismatch terms that defines least-squares fitting, we motivate a term in the objective function which penalizes variations in the tensor invariants of the reconstructed stress while preserving boundaries. By minimizing the objective function subject to appropriate physical constraints, we are able to efficiently reconstruct stress fields with localized structure from simulated and experimental substrate displacements. We provide a numerical method for setting up a discretized inverse problem that is solvable by standard convex optimization techniques. Our method incorporates the exact solution of the forward problem accurate to first-order finite-difference approximation in the stress tensor. Given newly-available high-resolution data, we motivate the use of distance-based cutoffs for data inclusion and find under loose regularity conditions the reconstruction error that results.

INTRODUCTION

The adhesion of cells and tissues to their environment has profound consequences on processes such as cell polarization [?], motion, division, differentiation, tissue morphology during development, and wound healing. Hence, quantifying how cells attach to an impart force on the surrounding material is an important technical challenge in cell biology.

Cell motility and response to signals have hitherto typically been studied in two-dimensional geometries in which cells are placed on a flat elastic substrate. Dynamic adhesion between the cells and the substrate are realized through *e.g.*, lamellapodia, filapodia, and dynamically reorganizing focal adhesions. Such structures are spatially localized, as shown in Fig. 1. Similarly, on larger length scales, a collection of cells can give rise to localized stress distributions. For example, the leading edge of a cell layer produces the pulling force that leads to migration in wound healing assays.

Dynamically varying force-generating structures are often small and difficult to image, especially without biochemical modification such as incorporation of fluorescent dyes. Therefore, other methods for inferring their positions and magnitudes have been developed. The simplest method relies on measuring the displacement of fiduciary markers, such as gold nanoparticles, embedded in the elastic substrate [?]. The measured displacements are an indirect probe of the force-generating structures, *e.g.*, focal adhesions. Any inversion method should be able to not only reconstruct the positions and magnitudes of the stress field, but should ideally be able to capture potentially sharp boundaries of the stress-generating structures.

./figures/Fig1.pdf

FIG. 1. A schematic of an isolated cell. (a) The boundary of the cell footprint is denoted by the dashed curve, the support of the stress field is represented by the red regions that impart a stress $\mathbf{F}(x, y)$ on the surface. Displacements $\mathbf{u}(\mathbf{r}_i)$ of the elastic medium are measured at position $\mathbf{r}_i = x_i\hat{x} + y_i\hat{y} + z_i\hat{z}$ (blue dots) that can be inside or outside the cell footprint, on the surface ($z_i = 0$), or below the surface ($z_i < 0$). (b). A perspective view of the elastic substrate and cellular footprint.

We develop a novel method for elastic stress source recovery using ideas developed for image segmentation. This class of methods relies on optimization that uses an L^1 regularization term in the objective function. This type of regularization term is not derived from a fundamental physical law, but represents a prior knowledge that the function to be recovered is sparse in content except near edges. In addition, the overall objective function will be constructed to obey physical constraints and symmetries.

In the next section, we review the standard linear equations of elasticity that describe the displacement field as a function of an arbitrary surface stress distribution. This model is then used to construct the data mismatch term in the objective function. We then motivate regularization and constraint terms in the full objective function.

Finally, we demonstrate our method using both simulated and experimental data. Our method provides good reconstruction of localized structures that exhibit desirable qualities such as the suppression of Gibbs ringing phenomenon at the boundaries of the stress structures.

ELASTIC MODEL

We first derive the linear elastic green's function associated with a point force applied to the surface of a semi-infinite half-space, as shown in Fig. 1(b). We assume that the elastic medium is infinite in both depth ($d \rightarrow \infty$) and lateral extent. The Green's function tensor defined in the domain $\mathcal{D} = \{(x, y, z) | x, y \in R, z \leq 0\}$ is given by

$$\mathbf{G}^0 = \begin{bmatrix} G_{xx}^0(x, y, z) & G_{xy}^0(x, y, z) & G_{xz}^0(x, y, z) \\ G_{yx}^0(x, y, z) & G_{yy}^0(x, y, z) & G_{yz}^0(x, y, z) \\ G_{zx}^0(x, y, z) & G_{zy}^0(x, y, z) & G_{zz}^0(x, y, z) \end{bmatrix} \quad (1)$$

where the components are explicitly [?]

$$G_{ss}^0(x, y, z) = \frac{1 + \nu}{2\pi E} \left[\frac{2(1 - \nu)R_{\perp} - z}{R_{\perp}(R_{\perp} - z)} + \frac{[2R_{\perp}(\nu R_{\perp} - z) + z^2]s^2}{R_{\perp}^3(R_{\perp} - z)^2} \right], \quad (2)$$

$$G_{zz}^0(x, y, z) = \frac{1 + \nu}{2\pi E} \left(\frac{2(1 - \nu)}{R_{\perp}} + \frac{z^2}{R_{\perp}^3} \right), \quad (3)$$

$$G_{xy}^0(x, y, z) = G_{yx} = \frac{1 + \nu}{2\pi E} \frac{[2R_{\perp}(\nu R_{\perp} - z) + z^2]xy}{R_{\perp}^3(R_{\perp} - z)^2}, \quad (4)$$

$$G_{sz,zs}^0(x, y, z) = \frac{1 + \nu}{2\pi E} \left(\frac{sz}{R_{\perp}^3} \pm \frac{(1 - 2\nu)s}{R_{\perp}(R_{\perp} - z)} \right). \quad (5)$$

and $s \equiv x, y$. The equation with \pm corresponds to G_{sz}^0 and G_{zs}^0 , respectively, and $R_{\perp} \equiv \sqrt{x^2 + y^2}$. The Young's modulus and Poisson ratio of the elastic substrate are denoted by E and ν , respectively. It is our choice throughout this manuscript to express stress in units of the elastic modulus, however, for matrigel, $E \approx 4 \pm 3 \times 10^2$ Pa and $\nu \approx 0.5$ [?].

The displacement of a material point at $(x, y, z \leq 0)$ in the medium due to a stress distribution \mathbf{F} is simply the convolution $\mathbf{u}(\mathbf{r}) \equiv [u_x \ u_y \ u_z]^T = \mathbf{G}^0 * \mathbf{F}$.

For our specific problem, we shall restrict the forces to surface stresses $\sigma_{x,y}$ that act on the plane perpendicular to the \hat{z} axis. We define the in-plane stress distribution, at depth z , as $\boldsymbol{\sigma}(x, y, z) = \sigma_{xz}(x, y, z)\hat{x} + \sigma_{yz}(x, y, z)\hat{y}$. The resulting surface-level displacement fields become

$$u_x(x, y) = \int_{\Omega} dx' dy' G_{xx}(x - x', y - y') \sigma_{xz}(x', y') + \int_{\Omega} dx' dy' G_{xy}(x - x', y - y') \sigma_{yz}(x', y') \quad (6)$$

$$u_y(x, y) = \int_{\Omega} dx' dy' G_{yx}(x - x', y - y') \sigma_{xz}(x', y') + \int_{\Omega} dx' dy' G_{yy}(x - x', y - y') \sigma_{yz}(x', y'), \quad (7)$$

where

$$G_{.,.}(x, y) = G_{.,.}^0(x, y, z = 0), \quad (8)$$

and by abuse of notation,

$$\sigma_{xz}(x, y) = \sigma_{xz}(x, y, z = 0) \quad \sigma_{yz}(x, y) = \sigma_{yz}(x, y, z = 0). \quad (9)$$

Note that tangential stresses can lead to displacement in the normal direction.

INVERSE PROBLEM

Here, we develop an objective function for which the minimizing solution provides a good approximation to the underlying stress field, while preserving discontinuities. The first component is simply a quadratic data mismatch term defined by the sum over the displacements measured at the N measurement positions at \mathbf{r}_i :

$$\Phi_{\text{data}}[\boldsymbol{\sigma}] = \sum_i^N |\mathbf{u}^{\text{data}}(\mathbf{r}_i) - \mathbf{u}(\mathbf{r}_i)|^2. \quad (10)$$

Since $\mathbf{u}^{\text{data}}(\mathbf{r}_i)$ is given, and $\mathbf{u}(\mathbf{r}_i)$, is given by Eqs. 6 and 7, this contribution to the objective function is a functional over the surface-stress function $\boldsymbol{\sigma}(\mathbf{r}_{\perp})$. For simplicity, we will assume that the data points are sampled over an uniform grid with coordinates given $\{(x_j, y_k) : j \in \{1, 2, \dots, J\}, k \in \{1, 2, \dots, K\}\}$.

In Eqs 6 and 7, we have restricted the domain of integration to lie within the cell footprint Ω , further emphasizing that $\boldsymbol{\sigma}$ has compact support. As a consequence of compact support, for a fixed, discretized approximation of σ_{xz}, σ_{yz} , the displacements can be obtained exactly by solving an equivalent system of linear equations of finite dimension.

Here we explicitly define this system of linear equations given a piecewise-affine approximation of the stress field. Let us consider the first-order approximation of σ_{xz} and

σ_{yz} using central finite differences, for $x \in [x_j - \delta x/2, x_j + \delta x/2) \cap y \in [y_j - \delta y/2, y_j + \delta y/2)$,

$$\begin{aligned}\sigma_{xz}(x, y) &= \sigma_{xz}(x_i, y_j) \\ &+ (x - x_i) \frac{\sigma_{xz}(x_{i+1}, y_j) - \sigma_{xz}(x_{i-1}, y_j)}{2\delta x} \\ &+ (y - y_j) \frac{\sigma_{xz}(x_i, y_{j+1}) - \sigma_{xz}(x_i, y_{j-1})}{2\delta y} \\ &+ \mathcal{O}(\delta x)^2 + \mathcal{O}(\delta y)^2,\end{aligned}\quad (11)$$

where i, j denotes a tuple of grid coordinates. In effect, we are performing sub-pixel interpolation of the stress where the stress is fully-determined by its values at the grid vertices.

We may now rewrite Eq. 6, for instance, to solve for the displacement at a location (x_n, y_m) , by decomposing the integral into a sum of integrals over grid cells

$$\begin{aligned}u_x(x_n, y_m) &= \\ &\sum_{(x_j, y_k) \in \Omega} \left\{ \left[\sigma_{xz}(x_j, y_k) - x_j \left(\frac{\sigma_{xz}(x_{j+1}, y_k) - \sigma_{xz}(x_{j-1}, y_k)}{2\delta x} \right) - y_k \left(\frac{\sigma_{xz}(x_j, y_{k+1}) - \sigma_{xz}(x_j, y_{k-1})}{2\delta y} \right) \right] \langle G_{xx} \rangle^{nmjk} \right. \\ &+ \left[\frac{\sigma_{xz}(x_{j+1}, y_k) - \sigma_{xz}(x_{j-1}, y_k)}{2\delta x} \right] \langle xG_{xx} \rangle^{nmjk} + \left[\frac{\sigma_{xz}(x_j, y_{k+1}) - \sigma_{xz}(x_j, y_{k-1})}{2\delta y} \right] \langle yG_{xx} \rangle^{nmjk} \\ &+ \left[\sigma_{yz}(x_j, y_k) - x_j \left(\frac{\sigma_{yz}(x_{j+1}, y_k) - \sigma_{yz}(x_{j-1}, y_k)}{2\delta x} \right) - y_k \left(\frac{\sigma_{yz}(x_j, y_{k+1}) - \sigma_{yz}(x_j, y_{k-1})}{2\delta y} \right) \right] \langle G_{xy} \rangle^{nmjk} \\ &\left. + \left[\frac{\sigma_{yz}(x_{j+1}, y_k) - \sigma_{yz}(x_{j-1}, y_k)}{2\delta x} \right] \int_{y_k - \delta y/2}^{y_k + \delta y/2} \langle xG_{xy} \rangle^{nmjk} + \left[\frac{\sigma_{yz}(x_j, y_{k+1}) - \sigma_{yz}(x_j, y_{k-1})}{2\delta y} \right] \langle yG_{xy} \rangle^{nmjk} \right\}, \quad (12)\end{aligned}$$

where

$$\begin{aligned}\langle g(x, y)G_{st} \rangle^{nmjk} &= \\ &\int_{y_k - \delta y/2}^{y_k + \delta y/2} \int_{x_j - \delta x/2}^{x_j + \delta x/2} g(x', y') G_{st}(x_n - x', y_m - y') dx' dy',\end{aligned}\quad (13)$$

except that at the edges where we use one-sided differences so that we are only differentiating within Ω . Explicit closed-form expressions for the integrals represented by Eq. ?? are given in the Supplemental Materials. A similar expression can be found for solving for u_y (not shown).

Regrouping terms, we can now define the linear system of equations for solving for u_x at all grid points simultaneously,

$$u_x^{nm} = X^{nmjk} \sigma_{xz}(x_j, y_k) + Y^{nmjk} \sigma_{yz}(x_j, y_k), \quad (14)$$

where summation is implied over each index tuple (j, k) ,

and the coefficient matrices are defined as

$$\begin{aligned}X^{nmjk} &= \langle G_{xx} \rangle^{nmjk} - \langle G_{xx} \rangle^{n,m,j-1,k} \frac{x_{j-1}}{2\delta x} \\ &+ \langle G_{xx} \rangle^{n,m,j+1,k} \frac{x_{j+1}}{2\delta x} - \langle G_{xx} \rangle^{n,m,j,k-1} \frac{y_{k-1}}{2\delta y} \\ &+ \langle G_{xx} \rangle^{n,m,j,k+1} \frac{y_{k+1}}{2\delta y} - \frac{\langle xG_{xx} \rangle^{n,m,j-1,k}}{2\delta x} \\ &+ \frac{\langle xG_{xx} \rangle^{n,m,j+1,k}}{2\delta x} - \frac{\langle yG_{xx} \rangle^{n,m,j,k-1}}{2\delta y} \\ &+ \frac{\langle yG_{xx} \rangle^{n,m,j,k+1}}{2\delta y}\end{aligned}\quad (15)$$

$$\begin{aligned}
Y^{n,m,j,k} = & \langle G_{xy} \rangle^{nmjk} - \langle G_{xy} \rangle^{n,m,j-1,k} \frac{x_{j-1}}{2\delta x} \\
& + \langle G_{xy} \rangle^{n,m,j+1,k} \frac{x_{j+1}}{2\delta x} - \langle G_{xy} \rangle^{n,m,j,k-1} \frac{y_{k-1}}{2\delta y} \\
& + \langle G_{xy} \rangle^{n,m,j,k+1} \frac{y_{k+1}}{2\delta y} - \frac{\langle xG_{xy} \rangle^{n,m,j-1,k}}{2\delta x} \\
& + \frac{\langle xG_{xy} \rangle^{n,m,j+1,k}}{2\delta x} - \frac{\langle yG_{xy} \rangle^{n,m,j,k-1}}{2\delta y} \\
& + \frac{\langle yG_{xy} \rangle^{n,m,j,k+1}}{2\delta y}. \tag{16}
\end{aligned}$$

From the equation-counting perspective, the system of equations is exactly determined given that one has at least as many measurement points as grid cells in the resolution that one wishes to reconstruct the stress field, provided that one is able to measure displacements in both principle directions. Even if one is able to measure both displacements, the problem may still be highly ill-conditioned since measurements are taken in the presence of noise at a finite precision. To resolve these issues, we introduce the concept of physically consistent regularization as applied to this problem.

Physical regularization

So far, the construction of the surface stress, even at the finite resolution where measurements are available, is ill-conditioned. We regularize this problem, by forcing the reconstruction to obey some physically-relevant characteristics of the surface stress. First, since we are assuming inertial effects are negligible, we require that the net force is zero, or that

$$\int_{\Omega} \sigma_{xz}(x, y) dx dy = \int_{\Omega} \sigma_{yz}(x, y) dx dy = 0. \tag{17}$$

Likewise, we require that there is no net torque, or that

$$\int_{\Omega} \sigma_{yz}(x, y) x dx dy = \int_{\Omega} \sigma_{xz}(x, y) y dx dy. \tag{18}$$

Finally, we would like to impose regularity on the reconstructed fields while preserving both rotational invariance and the sharp stress boundaries. To this end we employ a variant of a penalty used often in image processing applications, where we wish to penalize the L^1 norm of the variation in the fields, or the total variation. To do this in a manner that is consistent with the philosophy that rotation of the data should not affect the result, we penalize the total variation norm of the invariants of the stress tensor. In the case of two-dimensional tensors, of which the surface stress is an example, the tensor invariants are the trace

$$\text{Tr}(\boldsymbol{\sigma}) = \sigma_{xz} + \sigma_{yz} \tag{19}$$

and the determinant

$$\text{Det}(\boldsymbol{\sigma}) = \sigma_{xz}\sigma_{yz}. \tag{20}$$

Any regularization penalty imposed on the reconstruction problem must be a functional of these invariants in order to maintain rotational invariance, relative to the choice of observation frame, of the reconstructed stress tensor.

For this manuscript, we investigate penalty functionals on the trace of the stress tensor. In particular, we are interested in the L^1 norm of the trace

$$\Phi_{L^1(T_r)} = \int_{\Omega} |\sigma_{xz}(x, y) + \sigma_{yz}(x, y)| dx dy \tag{21}$$

and total variation norm of the trace

$$\Phi_{TV(T_r)} = \int_{\Omega} |\nabla(\sigma_{xz}(x, y) + \sigma_{yz}(x, y))| dx dy. \tag{22}$$

Using either of these expressions as the regularization norm Φ_{reg} suggests the penalized optimization problem

$$\hat{\boldsymbol{\sigma}} | \lambda = \arg \min_{\boldsymbol{\sigma}} \{ \Phi_{\text{data}}[\boldsymbol{\sigma}] + \lambda \Phi_{\text{reg}}[\boldsymbol{\sigma}] \}, \tag{23}$$

subject to the no-force and no-torque constraints mentioned above, where $\lambda > 0$ is a tunable parameter. This problem is in a standard form that is directly solvable using a variety of optimization routines. In our implementation, we use a second-order quadratic cone solver.

Reducing computation by using a cut-off

To reduce the size of the system of equations described in Eqs. 14–16, we note that the Green's function falls off at a rate of $|\mathbf{r}|^{-1}$. However, when combined with the zero-force constraint, the relationship between the displacements and the support of the stress field falls off at the much quicker rate of $|r|^{-2}$, under a set of reasonable assumptions that are consistent with the choice of regularization that we have made.

Lemma 1. *Let $\Omega = \text{supp}(\boldsymbol{\sigma}) \subset \mathbb{R}^2$ be compact, and assume that $\boldsymbol{\sigma} \in L^1(\Omega)$. For a fixed $\mathbf{x} \notin \Omega$, denote $D(\mathbf{x}) = \inf\{ \|\mathbf{x} - \mathbf{y}\| : \mathbf{y} \in \Omega \}$. Then, for \mathbf{x} where $D(\mathbf{x}) \geq R > 0$,*

$$|u_x(\mathbf{x})| \leq \frac{C_x \|\boldsymbol{\sigma}\|_1}{R^2} \tag{24}$$

and

$$|u_y(\mathbf{x})| \leq \frac{C_y \|\boldsymbol{\sigma}\|_1}{R^2} \tag{25}$$

for some constants C_x, C_y .

Lemma 2. *Let $\tilde{\boldsymbol{\sigma}}$ be an affine approximation to $\boldsymbol{\sigma} \in C^s(\Omega)$ for $s \in \mathbb{Z}^+$, and $\tilde{\mathbf{u}}$ be the corresponding displacement field completed from the approximate stress field. Then,*

$$|\tilde{\mathbf{u}} - \mathbf{u}| \leq C(\delta x)^2 \tag{26}$$

The decay of the influence of stress on the system provides justification for setting distance-based cut-offs of the linear system. The effect of the cut-off is to limit the left-hand side of Eq. 14 to only locations within some maximal distance R from the outline of the cell. The error in the solution of the inverse problem is dependent on the precision of the observations, the physical constants that describe the medium, and the maximum magnitude of the stress.

Theorem 3. Denote $\varepsilon^R(\mathbf{r}) = \hat{\sigma}^R(\mathbf{r}) - \sigma(\mathbf{r})$ for $\mathbf{r} \in \Omega$, where $\sigma_{xz} \in L^1(\Omega)$, and $\hat{\sigma}^R(\mathbf{r})$ is the reconstructed stress field found by solving the optimization problem of Eq. 23 using only the displacement data within a maximal distance of R from the cell. Then,

$$\sup |\hat{\sigma}^R(\mathbf{r}) - \hat{\sigma}^\infty(\mathbf{r})| \leq \frac{C}{R^2} \quad (27)$$

Proof. TODO... result needs refinement \square

RESULTS

We implemented our regularized inversion method in Python version 3.5, where optimization is performed using the `cvxpy` package with the `ecos` solver. Our implementation is available at <https://github.com/joshchang/tractionforce>.

First we tested our method on simulated data consisting of two different force- and torque-free test stress fields. The first test stress field we consider is

$$\sigma_{rz}(r, \theta) = f_r \sin(m\theta) \quad \sigma_{\theta z}(r, \theta) = f_\theta \cos(n\theta), \quad (28)$$

for $a < r < 1$, and zero otherwise. Here, m, n are odd integers and if we normalize the stresses by the Young's modulus E , f_r and f_θ are constants.

The second stress field we test consists of four separated circular stress pads, or focal adhesions, with radii $r_1 = 1/5$, $r_2 = 1/6$, $r_3 = 1/8$, and $r_4 = 1/4$, and centers at positions $(x_1, y_1) = (-1, -1/2)$, $(x_2, y_2) = (-5/4, 0)$, $(x_3, y_3) = (2, 1)$, and $(x_4, y_4) = (0, 1)$. The pads 1, 2, and 4 are connected as shown, while pad 3 is connected only to pad 1. The tensions along these connections give rise to surface stresses imparted by the pads onto the substrate. Within each of the pads, except for pad 4, the foci will be uniformly distributed. For pad 4, we will assume that the filaments connecting it with pad 2 are distributed according to a cone-like density function. The stresses under each patch i are decomposed into contributions arising from tensions with connected patches j :

$$\sigma_{42} = -g_{42}(r)\hat{y}, \quad \sigma_{24} = \hat{y} \frac{2\pi}{\pi r_2^2} \int_0^{r_4} r g_{42}(r) dr = \frac{3}{4} \bar{g}_{42} \hat{y} \quad (29)$$

$$\sigma_{14} = f_{14}\hat{x} + g_{14}\hat{y}, \quad \sigma_{41} = -\left(\frac{4}{5}\right)^2 \sigma_{14} \quad (30)$$

$$\sigma_{12} = f_{12}\hat{x} - g_{12}\hat{y}, \quad \sigma_{21} = -\left(\frac{6}{5}\right)^2 \sigma_{12} \quad (31)$$

$$\sigma_{13} = f_{13}\hat{x} + g_{13}\hat{y}, \quad \sigma_{31} = -\left(\frac{8}{5}\right)^2 \sigma_{13} \quad (32)$$

where we have defined σ_{ij} in units of the Young's modulus E and $f_{ij}, g_{ij} > 0$ are all dimensionless constants. The normalized stresses σ_{ij} are nonzero only in the disk r_i . All stress distributions are constant inside the disks except for

$$g_{42}(r) = \bar{g}_{42} \left(1 - \frac{r}{r_4}\right), \quad (33)$$

where \bar{g}_{42} is a constant that sets the maximum value of $g_{42}(r = 0)$. The way to interpret this physically is that the multiple filaments that connect patch 4 to patch 2 are uniformly attached under patch 2, but *not* under patch 4. The density of attachments linearly decrease from the center of patch 4. This variation in attachment density arises only for those filaments that attach patch 4 to patch 2, and only at patch 4. The all other filaments are assumed to attach uniformly under each pad. In this test case, the tension between pads 1 and 3 is $T_{13} = (1/5)^2 \sqrt{f_{13}^2 + g_{13}^2}$. Both test fields, along with possible cell footprint boundaries are shown in Fig. 2.

RESULTS AND PLOTS FOR TEST STRESS FIELDS:

Next, we consider experimental displacements resulting from stress generated by a single cell. The surface displacements were measured using Hilbert space dynamometry which uses phase information of the periodic signal arising from a chemically patterned grid on the substrate [?]. Both x and y -displacements at a resolution of the patterned grid spacing can be measured, as shown in Fig. 4

The results of reconstruction of the stress field using our method are shown in Fig. 5.

We also compared reconstruction of the surface stress using our rotationally invariant norms of Eq. 21 and Eq. 22 against alternate isotropic norms. As an alternative to the L^1 norm on the trace we compared

$$\Phi_{L1} = \int_{\Omega} |\sigma_{xz}(x, y) + \sigma_{yz}(x, y)| d\mathbf{r}, \quad (34)$$

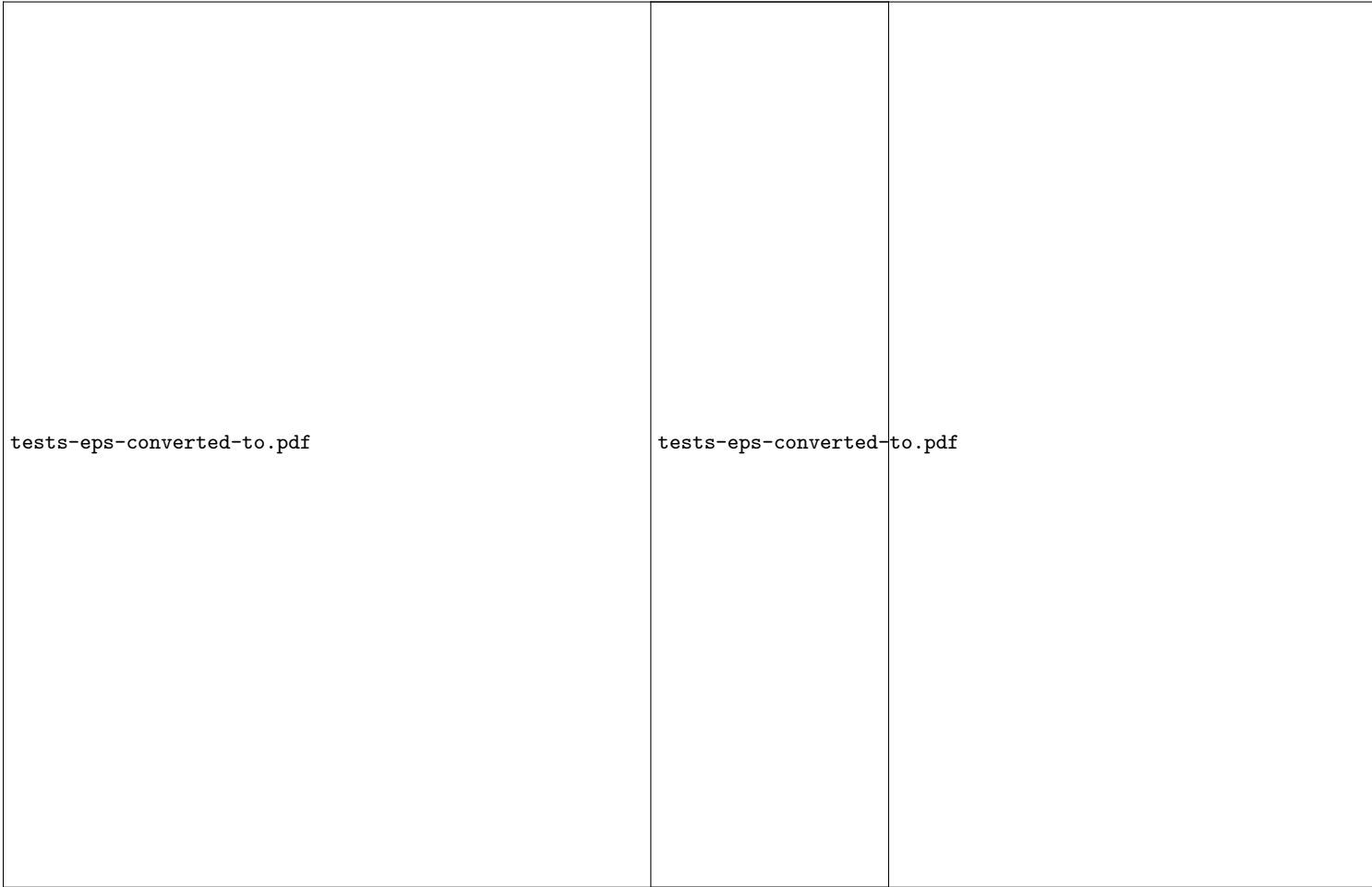


FIG. 2. **Test stress fields.** (a) An annular stress distribution containing forces in the θ and r directions. (b) Four focal adhesions under mutual tension as by the green lines representing filaments. The red borders represent the extent of the cell footprint and can be determined experimentally as part of the imaging. Mathematically, the cell boundary forms the basis for a constraint on the stress distribution and we explore the quality of inversion depends on this constraint.

and as alternatives to the total variation on the trace we looked at

$$\Phi_{TV_1} = \int_{\Omega} (|\nabla \sigma_{xz}(x, y)| + |\nabla \sigma_{yz}(x, y)|) \, d\mathbf{r} \quad (35)$$

and

$$\Phi_{TV_2} = \int_{\Omega} (|\partial_x \sigma_{xz}| + |\partial_y \sigma_{xz}| + |\partial_x \sigma_{yz}| + |\partial_y \sigma_{yz}|) \, d\mathbf{r}. \quad (36)$$

The adjustable parameter λ was chosen in each instance by examining the balance between data mismatch and regularity using trade-off curves shown in Fig. 5, and taking the value for λ that yields a point farthest away from the line segment joining the ends of the plot. In

tests-eps-converted-to.pdf

FIG. 3. **Inversion results for test stress fields.** (a) Inversion for the annular stress field with $m = 4$, $n = 2$ and ...using different cell boundaries....

Fig. 5, the chosen value of λ corresponds to the given balance between regularity and data fidelity marked by the red circle. The solution corresponding to this particular value of λ is shown in the middle column on the right. For reference, under-regularized solutions, corresponding to the green circle in the trade-off plot, and over-regularized solutions, corresponding to black circle, are also given. Each row in Fig. 5 corresponds to the use of a different regularization penalty functional. In all of these reconstructions, we have imposed that the surface stress is both force-free and torque free, and also that the support of the stress is within given cell boundaries.

To explore the effect of the constraints on our reconstructions, we systematically removed them in solving the rotationally invariant L^1 regularized problem. In Fig. 6, we present reconstructions where net torque is free to vary but force is constrained, where net force is free to vary but torque is constrained, and where net torque and force are both free to vary. In each of these reconstruc-

./figures/fig0a.png

FIG. 4. **Bright field image and displacements.** (a) Raw bright field image of a mesenchymal stem cell. The cell footprint boundary is estimated from segmentation. (b) and (c) The x - and y -displacement fields at the surface of the substrate.

tions the unconstrained quantity did not sum to zero, as desired.

Additionally, our reconstructions are implicitly constrained by the assumption of compact support where the support of the stress tensor is within the cell boundary. Examining Fig. 5, it appears that this constraint is active as much of the stress is concentrated at boundaries. In Fig. 7, we loosened the boundary constraint by allowing the support of the stress to fall within 10 pixels of the cell boundary.

APPLY THESE LAST TWO ANALYSES TO TEST DATA INSTEAD OF REAL DATA?

DISCUSSION AND CONCLUSIONS

We have presented a comprehensive method for solving the inverse problem of surface stress reconstruction that incorporates physical knowledge as constraints. Under piecewise affine approximations of the stress tensor, we provided an exact solution to the forward problem as a system of linear equations. Using the multipole expansion, we motivated the use of a cut-off in the solution of the forward problem thereby decreasing both the computational complexity of the problem and the memory requirements. The numerical stability of the problem was also improved using regularization which obeys the geometric constraint that the problem should be rotationally invariant.

Our method exploits physical constraints that allows for superior reconstruction of complex surface stress fields. We also showed how the known footprint boundary can impact the reconstruction. In general, footprints

that extend beyond the extend of the support of the stress field worsens the inversion, allowing for “leakage” of stress beyond its actual support. Our method can naturally apply to related systems such as scratch wound assays.

Integrals

In this section we provide closed-form expressions for the integrals represented by Eq. 13. Let $\Delta x_{nj}^+ = x_n - (x_j + \delta x/2)$, $\Delta x_{nj}^- = x_n - (x_j - \delta x/2)$, $\Delta y_{mk}^+ = y_m - (y_k + \delta y/2)$, and $\Delta y_{mk}^- = y_m - (y_k - \delta y/2)$. Then, we have the averaged Greens functions

$$\begin{aligned} \langle G_{uv} \rangle^{nmjk} = & f_{uv}(\Delta x_{nj}^+, \Delta y_{mk}^+) - f_{uv}(\Delta x_{nj}^+, \Delta y_{mk}^-) \\ & - f_{uv}(\Delta x_{nj}^-, \Delta y_{mk}^+) + f_{uv}(\Delta x_{nj}^-, \Delta y_{mk}^-) \end{aligned} \quad (37)$$

where

$$\begin{aligned} f_{xx}(x, y) = & \frac{\nu + 1}{\pi E} \left[x(1 - \nu) \log \left(\sqrt{x^2 + y^2} + y \right) \right. \\ & \left. + y \log \left(\sqrt{x^2 + y^2} + x \right) - y \right] \end{aligned} \quad (38)$$

$$\begin{aligned} f_{yy}(x, y) = & \frac{\nu + 1}{\pi E} \left[y(1 - \nu) \log \left(\sqrt{x^2 + y^2} + x \right) \right. \\ & \left. + x \log \left(\sqrt{x^2 + y^2} + y \right) - x \right] \end{aligned} \quad (39)$$

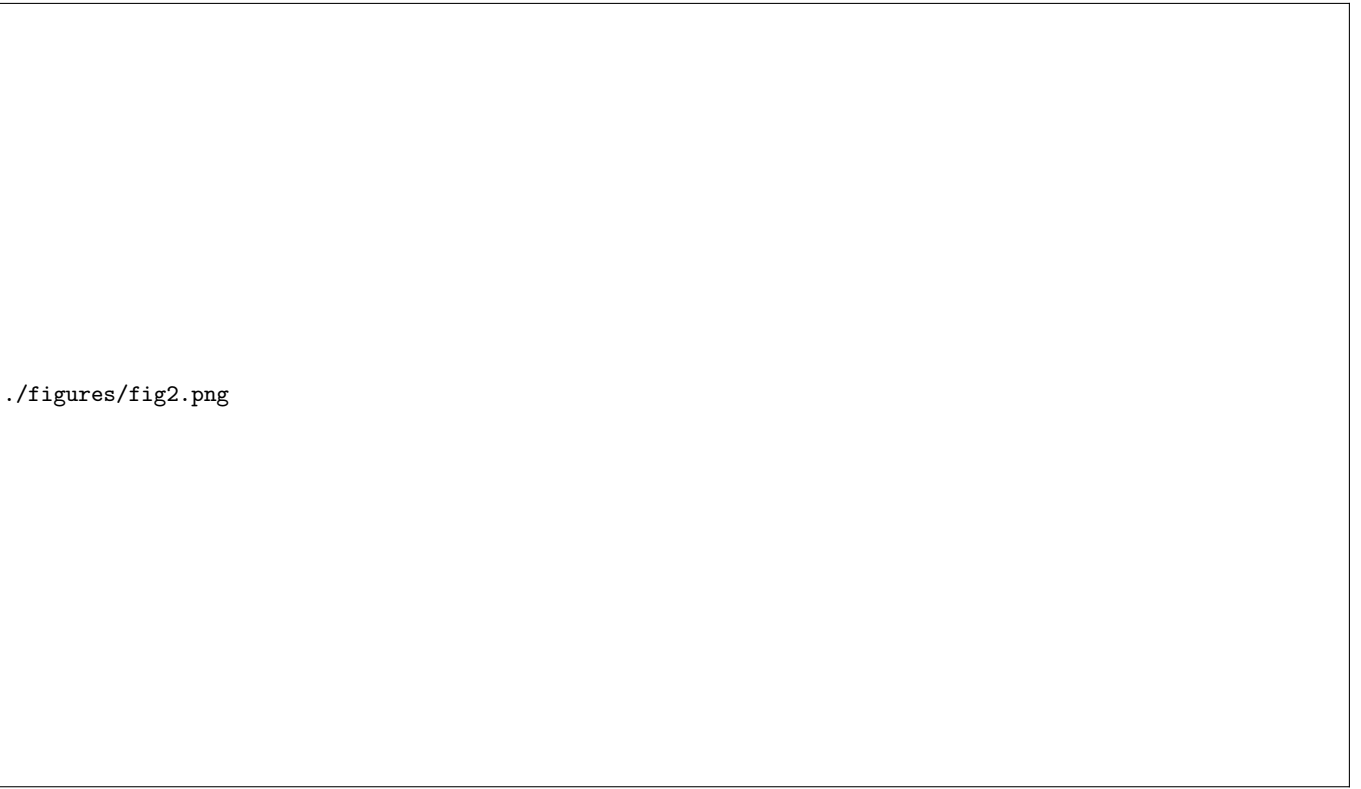
$$f_{xy}(x, y) = -\frac{\nu(\nu + 1)}{\pi E} \sqrt{x^2 + y^2}. \quad (40)$$

The first moments follow

$$\begin{aligned} \langle x G_{xx}(x, y) \rangle^{nmjk} = & \left[f_{xx}(\Delta x_{nj}^+, \Delta y_{mk}^+) - f_{xx}(\Delta x_{nj}^+, \Delta y_{mk}^-) \right. \\ & \left. - f_{xx}(\Delta x_{nj}^-, \Delta y_{mk}^+) + f_{xx}(\Delta x_{nj}^-, \Delta y_{mk}^-) \right] x_n \\ & - \left[f_{xx}^x(\Delta x_{nj}^+, \Delta y_{mk}^+) - f_{xx}^x(\Delta x_{nj}^+, \Delta y_{mk}^-) \right. \\ & \left. - f_{xx}^x(\Delta x_{nj}^-, \Delta y_{mk}^+) + f_{xx}^x(\Delta x_{nj}^-, \Delta y_{mk}^-) \right], \end{aligned} \quad (41)$$

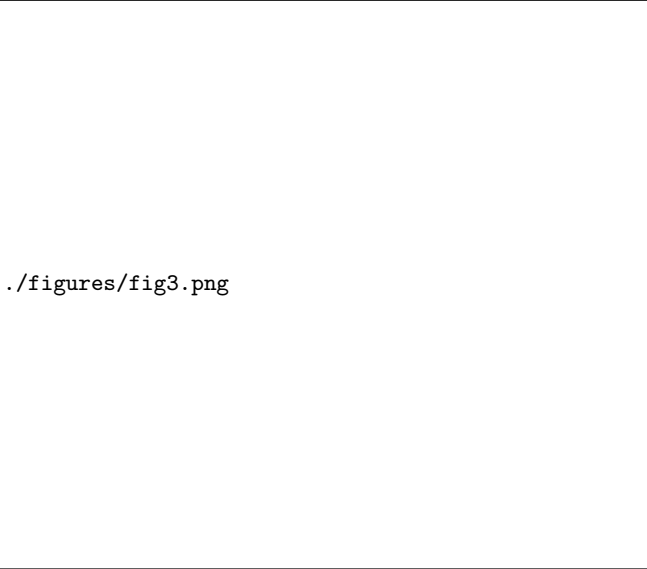
where

$$\begin{aligned} f_{xx}^x(x, y) = & \frac{\nu + 1}{2\pi E} \left[(\nu + 1)y \sqrt{x^2 + y^2} \right. \\ & \left. - (\nu - 1)x^2 \log \left(\sqrt{x^2 + y^2} + y \right) \right], \end{aligned} \quad (42)$$



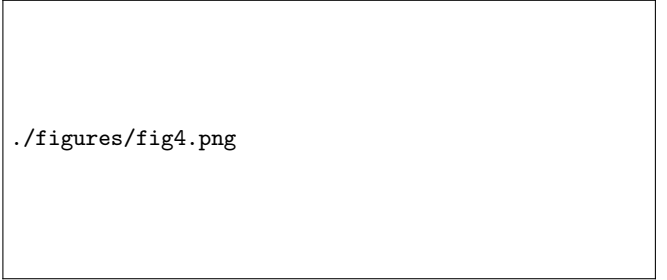
./figures/fig2.png

FIG. 5. **Reconstruction of experimental surface stress field** for various choices of regularization. The first and third rows are physically-consistent regularizations. The best reconstruction balances regularity and data matching and corresponds to the value for λ that is near a phase transition in the trade off plot between these two penalties (circled in red). The under-regularized solution corresponds to the point circled in green and the over-regulated solution corresponds to the point circled in black.



./figures/fig3.png

FIG. 6. **Omission of constraints** leads to solutions that do not naturally obey the constraints. Plotted are best reconstructions under the isotropic L^1 penalty and the difference between these reconstructions and the corresponding fully constrained reconstruction of Fig. 5.



./figures/fig4.png

FIG. 7. **Boundary constraint weakening** leads to solutions where the support does not fall naturally within the cell boundary. In the unconstrained reconstruction, the support of the stress was allowed to extend an additional 10 pixels outside of the cell boundary. The reconstruction did not naturally limit its support to the cell boundary.

$$\begin{aligned}
\langle yG_{xx}(x, y) \rangle^{nmjk} = & \left[f_{xx}(\Delta x_{nj}^+, \Delta y_{mk}^+) - f_{xx}(\Delta x_{nj}^+, \Delta y_{mk}^-) \right. \\
& - f_{xx}(\Delta x_{nj}^-, \Delta y_{mk}^+) + f_{xx}(\Delta x_{nj}^-, \Delta y_{mk}^-) \Big] y_m \\
& - \left[f_{xx}^y(\Delta x_{nj}^+, \Delta y_{mk}^+) - f_{xx}^y(\Delta x_{nj}^+, \Delta y_{mk}^-) \right. \\
& - f_{xx}^y(\Delta x_{nj}^-, \Delta y_{mk}^+) + f_{xx}^y(\Delta x_{nj}^-, \Delta y_{mk}^-) \Big], \tag{43}
\end{aligned}$$

where

$$\begin{aligned}
f_{xx}^y(x, y) = & \frac{\nu+1}{2\pi E} \left[y^2 \log(\sqrt{x^2+y^2}+x) \right. \\
& \left. - \sqrt{x^2+y^2} \left((2\nu-1)x + \frac{1}{2}\sqrt{x^2+y^2} \right) \right], \tag{44}
\end{aligned}$$

and

$$\begin{aligned}
\langle xG_{xy}(x, y) \rangle^{nmjk} = & \left[f_{xy}(\Delta x_j^-, \Delta y_k^+) - f_{xy}(\Delta x_j^-, \Delta y_k^-) \right. \\
& - f_{xy}(\Delta x_j^+, \Delta y_k^+) + f_{xy}(\Delta x_j^+, \Delta y_k^-) \Big] x_n \\
& - \left[f_{xy}^x(\Delta x_j^+, \Delta y_j^+) - f_{xy}^x(\Delta x_j^+, \Delta y_j^-) \right. \\
& - f_{xy}^x(\Delta x_j^-, \Delta y_j^+) + f_{xy}^x(\Delta x_j^-, \Delta y_j^-) \Big] \tag{45}
\end{aligned}$$

where

$$\begin{aligned}
f_{xy}^x(x, y) = & \frac{\nu(\nu+1)}{\pi E} \left[\frac{y^2}{2} \log(\sqrt{x^2+y^2}+x) \right. \\
& \left. - \frac{1}{4}\sqrt{x^2+y^2}(\sqrt{x^2+y^2}+2x) \right]. \tag{46}
\end{aligned}$$

All of these expressions may be found through direct iterated evaluation of the integrals, noting that as long as $n \neq m$ or $j \neq k$ the integrand (effectively the Green's function) is bounded, hence making Fubini's theorem applicable given the compactly supported domains of integration.

In the special case where $n = m$ and $j = k$, these formulae also hold. This fact is found by decomposing the integration domain to exclude the origin, for instance in the manner

$$\int_{-\Delta y/2}^{\Delta y/2} \int_{-\Delta x/2}^{\Delta x/2} \mathbf{dr} = \lim_{\varepsilon \rightarrow 0} \left(\int_{\varepsilon}^{\Delta y/2} + \int_{-\Delta y/2}^{-\varepsilon} \right) \int_{\Delta x/2}^{\Delta x/2} \mathbf{dr}. \tag{47}$$

Since the antiderivatives of Eqs 38, 39, 40, 42, 44, and 46 all have well-defined limits with only removable discontinuities at the origin, integrals of the Green's functions defined through Eq. 47 all converge about the origin and the equations above also hold in the case where $n = m$ and $j = k$.

Proof of Lemma 1

Proof. Note that u_x and u_y are symmetric in form. Hence, it will suffice to prove just one of these assertions. Eq. 6 can be written as

$$\begin{aligned}
u_x(\mathbf{r}) = & \frac{1+\nu}{\pi E} \int \frac{\mathbf{dr}}{|\mathbf{r}-\mathbf{r}'|} \left\{ \left[\frac{\nu(x-x')^2}{|\mathbf{r}-\mathbf{r}'|^2} + 1 - \nu \right] \sigma_x(\mathbf{r}') \right. \\
& \left. + \nu \frac{(x-x')(y-y')}{|\mathbf{r}-\mathbf{r}'|^2} \sigma_y(\mathbf{r}') \right\} \\
= & \frac{1+\nu}{\pi E} \int \frac{\mathbf{dr}'}{|\mathbf{r}-\mathbf{r}'|} \rho_x(\mathbf{r}, \mathbf{r}') \tag{48}
\end{aligned}$$

where $\rho_x(\mathbf{r}, \mathbf{r}')$ is $\mathcal{O}(1)$ as $|\mathbf{r}| \rightarrow \infty$. Without loss of generality, we assume that the coordinate system is centered at some point $\mathbf{0} \in \Omega$. The Euclidean distances can then be represented through the binomial expansion,

$$\begin{aligned}
\frac{1}{|\mathbf{r}-\mathbf{r}'|^p} = & \frac{1}{|\mathbf{r}|^p} \frac{1}{\left(1 - \frac{2\mathbf{r} \cdot \mathbf{r}' - |\mathbf{r}'|^2}{|\mathbf{r}|^2}\right)^p} \\
= & \frac{1}{|\mathbf{r}|^p} \sum_{k=0}^{\infty} \binom{p+k-1}{k} \left(\underbrace{\frac{2\mathbf{r} \cdot \mathbf{r}' - |\mathbf{r}'|^2}{|\mathbf{r}|^2}}_{\mathcal{O}(|\mathbf{r}|^{-1})} \right)^k, \tag{49}
\end{aligned}$$

where the series converges due to the fact that $|\mathbf{r}| > |\mathbf{r}'|$, since $\mathbf{r} \notin \Omega$, whereas $\mathbf{r}' \in \Omega$. Plugging this series into the last line of Eq. 48, one sees that in order to show that the magnitude of $u_x(\mathbf{r})$ is $\mathcal{O}(|\mathbf{r}|^{-2})$, it suffices to show that $\int \rho(\mathbf{r}, \mathbf{r}') \mathbf{dr}' \leq \mathcal{O}(|\mathbf{r}|^{-1})$.

Using the fact that $\int \boldsymbol{\sigma}(\mathbf{r}) \mathbf{dr} = \mathbf{0}$, one finds that

$$\begin{aligned}
\int \rho(\mathbf{r}, \mathbf{r}') \mathbf{dr}' = & \int (1-\nu) \sigma_x(\mathbf{r}') \mathbf{dr}' \\
& + \nu \int \left[\frac{(x-x')^2}{|\mathbf{r}-\mathbf{r}'|^2} \sigma_x(\mathbf{r}') + \frac{(x-x')(y-y')}{|\mathbf{r}-\mathbf{r}'|^2} \sigma_y(\mathbf{r}') \right] \mathbf{dr}' \\
= & \frac{\nu}{|\mathbf{r}|^2} \int \left[(x-x')^2 \sigma_x(\mathbf{r}') + (x-x')(y-y') \sigma_y(\mathbf{r}') \right] \\
& \times \sum_{k=0}^{\infty} \left[\frac{2\mathbf{r} \cdot \mathbf{r}' - |\mathbf{r}'|^2}{|\mathbf{r}|^2} \right]^k \mathbf{dr}'. \tag{50}
\end{aligned}$$

Expanding the leading order term of this expression, we

see that

$$\begin{aligned}
& \int \rho(\mathbf{r}, \mathbf{r}') d\mathbf{r}' \\
&= \frac{\nu}{|\mathbf{r}|^2} \int \left[(x - x')^2 \sigma_x(\mathbf{r}') + (x - x')(y - y') \sigma_y(\mathbf{r}') \right] \\
&\quad \times [1 + \mathcal{O}(|\mathbf{r}|^{-1})] d\mathbf{r}' \\
&= \frac{\nu}{|\mathbf{r}|^2} \left[-2x \int x' \sigma_x(\mathbf{r}') d\mathbf{r}' + \int x'^2 \sigma_x(\mathbf{r}') d\mathbf{r}' \right. \\
&\quad - x \int y' \sigma_y(\mathbf{r}') d\mathbf{r}' - y \int x' \sigma_y(\mathbf{r}') d\mathbf{r}' \\
&\quad \left. + \int x' y' \sigma_y(\mathbf{r}') d\mathbf{r}' \right] [1 + \mathcal{O}(|\mathbf{r}|^{-1})] \\
&= \mathcal{O}(|\mathbf{r}|^{-1}).
\end{aligned}$$

Hence, it is evident that this integral of $\mathcal{O}(|\mathbf{r}|^{-2})$, where to the leading order we have

$$\begin{aligned}
u_x(\mathbf{r}) &= \frac{1 + \nu}{\pi E |\mathbf{r}|^2} \left[-2 \frac{x}{|\mathbf{r}|} \int x' \sigma_x(\mathbf{r}') d\mathbf{r}' - \frac{x}{|\mathbf{r}|} \int y' \sigma_y(\mathbf{r}') d\mathbf{r}' \right. \\
&\quad \left. - \frac{y}{|\mathbf{r}|} \int x' \sigma_y(\mathbf{r}') d\mathbf{r}' + 1 - \nu \right], \quad (51)
\end{aligned}$$

ignoring the fact that this expression also contains some information at lower orders. \square

Proof of Lemma 2

Let $\tilde{\sigma}$ be the piecewise affine approximation of the stress field σ , and $\mathbf{r} \in \Omega_{jk}$. Then, by the Taylor remainder theorem, one sees that

$$\sigma_x(\mathbf{r}) - \tilde{\sigma}_x(\mathbf{r}) = \frac{1}{2} (\mathbf{r} - \mathbf{r}_{jk})^\top \mathbf{d}^2 \sigma_x(\mathbf{c}_{jk}) (\mathbf{r} - \mathbf{r}_{jk})$$

and

$$\sigma_y(\mathbf{r}) - \tilde{\sigma}_y(\mathbf{r}) = \frac{1}{2} (\mathbf{r} - \mathbf{r}_{jk})^\top \mathbf{d}^2 \sigma_y(\mathbf{a}_{jk}) (\mathbf{r} - \mathbf{r}_{jk})$$

where $\mathbf{c}_{jk}, \mathbf{a}_{jk} \in \Omega_{jk}$ and $\mathbf{r}_{jk} \in \Omega_{jk}$ is the point about which interpolation is performed. Hence,

$$\begin{aligned}
u_x(\mathbf{r}) - \tilde{u}_x(\mathbf{r}) &= \sum_{j,k} \int_{\Omega_{jk}} G_{xx}(\mathbf{r}, \mathbf{r}') (\sigma_x(\mathbf{r}') - \tilde{\sigma}_x(\mathbf{r}')) d\mathbf{r}' \\
&\quad + \sum_{j,k} \int_{\Omega_{jk}} G_{xy}(\mathbf{r}, \mathbf{r}') (\sigma_y(\mathbf{r}') - \tilde{\sigma}_y(\mathbf{r}')) d\mathbf{r}' \\
&= \sum_{j,k} \frac{\mathbf{d}_{xx}^2 \sigma_x(\mathbf{c}_{jk})}{2} \int_{\Omega_{jk}} G_{xx}(x - x', y - y') (x' - x_j)^2 d\mathbf{r}' \\
&\quad + \sum_{j,k} \frac{\mathbf{d}_{xy}^2 \sigma_x(\mathbf{c}_{jk})}{2} \int_{\Omega_{jk}} G_{xx}(x - x', y - y') (x' - x_j)(y' - y_k) d\mathbf{r}' \\
&\quad + \sum_{j,k} \frac{\mathbf{d}_{yy}^2 \sigma_x(\mathbf{c}_{jk})}{2} \int_{\Omega_{jk}} G_{xx}(x - x', y - y') (y' - y_k)^2 d\mathbf{r}' \\
&\quad + \sum_{j,k} \frac{\mathbf{d}_{xx}^2 \sigma_y(\mathbf{a}_{jk})}{2} \int_{\Omega_{jk}} G_{xy}(x - x', y - y') (x' - x_j)^2 d\mathbf{r}' \\
&\quad + \sum_{j,k} \frac{\mathbf{d}_{xy}^2 \sigma_y(\mathbf{a}_{jk})}{2} \int_{\Omega_{jk}} G_{xy}(x - x', y - y') (x' - x_j)(y' - y_k) d\mathbf{r}' \\
&\quad + \sum_{j,k} \frac{\mathbf{d}_{yy}^2 \sigma_y(\mathbf{a}_{jk})}{2} \int_{\Omega_{jk}} G_{xy}(x - x', y - y') (y' - y_k)^2 d\mathbf{r}' \quad (52)
\end{aligned}$$

Proof of Theorem 3

Consider the data penalty term Φ_{data} of the optimization problem

$$\Phi_{\text{data}}[\sigma] = \sum_{i=1}^M |\mathbf{u}^{\text{data}}(\mathbf{r}_i) - \mathbf{u}(\mathbf{r}_i)|^2 + \sum_{i=M+1}^N |\mathbf{u}^{\text{data}}(\mathbf{r}_i) - \mathbf{u}(\mathbf{r}_i)|^2$$

where the first M data points are all within a maximal cut off distance of R within the boundary of the cell and the remaining $N - M$ datapoints lie outside this distance.